

Modeled source apportionment of black carbon particles coated with a light-scattering shell

Aki Virkkula

Finnish Meteorological Institute

Helsinki, Finland

Abstract

The Aethalometer model has been used widely for estimating the contributions of fossil fuel emissions and biomass burning to equivalent black carbon (eBC). The calculation is based on measured absorption Ångström exponents (α_{abs}). The interpretation of α_{abs} is ambiguous since it is well-known that it not only depends on the dominant absorber but also on the size and internal structure of the particles, core size and shell thickness. In this work the uncertainties of the Aethalometer-model-derived apparent fractions of absorption by eBC from fossil fuel and biomass burning are evaluated with a core-shell Mie model. Biomass-burning fractions (BB(%)) were calculated for pure and coated single BC particles, for lognormal unimodal and bimodal size distributions of BC cores coated with ammonium sulfate, a scattering-only material. BB(%) was very seldom 0% even though BC was the only absorbing material in the simulations. The shape of size distribution plays an important role. Narrow size distributions result in higher α_{abs} and BB(%) values than wide size distributions. The sensitivity of α_{abs} and BB(%) to variations in shell volume fractions is the highest for accumulation mode particles. This is important because that is where the largest aerosol mass is. For the interpretation of absorption Ångström exponents it would be very good to measure BC size distributions and shell thicknesses together with the wavelength dependency of absorption.

1. Introduction

Incomplete combustion of organic fuels results in emission of light-absorbing carbon (LAC) particles that contain both black carbon (BC) and brown carbon (BrC). BrC is light-absorbing organic matter in atmospheric aerosols of various origins e.g., soil humics, humic-like substances (HULIS), tarry materials from combustion, bioaerosols (Andreae and Gelencser, 2006; Laskin et al., 2015). BrC can significantly absorb solar radiation in the ultraviolet–visible (uv–vis) wavelength range ($\lambda \approx 300 - 800$ nm). The

radiative effects of BC and BrC vary in time during atmospheric aging. For many combustion sources the absorbance in fresh emission is almost completely caused by BC particles but during atmospheric transport they often get coated with some light-scattering compounds, for instance ammonium sulfate or light-absorbing organic carbon, BrC. For some sources (e.g. biomass burning) BrC may contribute substantially to light-absorption already in the directly emitted aerosols and either increase or decrease during aging. Thus, BrC is highly time-dependent as it's composition and absorption properties change during atmospheric oxidation processes (Laskin et al., 2015).

The absorption coefficient σ_{ap} is approximately proportional to the power function $\lambda^{-\alpha_{abs}}$ where λ is the wavelength and α_{abs} is the absorption Ångström exponent. α_{abs} is generally used to distinguish aerosol types: for pure BC particles $\alpha_{abs} \approx 1$ while other light absorbing aerosols (BrC, soil dust) it is clearly > 1 (e.g., Kirchstetter et al., 2004; Bond and Bergstrom, 2006; Bergstrom et al., 2007; Moosmüller et al., 2011; Kirchstetter and Thatcher, 2012; Lack et al., 2012; Bond et al., 2013; Saleh et al., 2013; Laskin et al., 2015; Valenzuela et al., 2015; Devi et al., 2016). The method has been used not only for in situ absorption measurements but also for interpreting absorption coefficients retrieved from remote sensing measurements, such as the AERONET (e.g., Russell et al., 2010; Arola et al., 2011; Chung et al., 2012; Cazorla et al., 2013; Feng et al., 2013; Schuster et al., 2016; Wang et al., 2016).

One of the instruments used for measuring black carbon concentrations is the Aethalometer that collects aerosol on a filter tape, measures changes in light attenuation in the wavelength range of 370 – 950 nm and calculates the equivalent black carbon (eBC) concentrations. The data are used also to calculate α_{abs} and to estimate the contributions of fossil fuel emissions and biomass burning to eBC. The Aethalometer model (Sandradewi et al., 2008a) is probably the most widely-used method for this and it is even calculated automatically in the new Aethalometer model AE33. It is there assumed that the absorption Ångström exponents are $\alpha_{ff} = 1$ and $\alpha_{bb} = 2$ for eBC from fossil fuel and biomass burning, respectively. These are the default settings in the AE33, but also different α_{ff} and α_{bb} values have been used (Sandradewi et al., 2008b; Herich et al., 2011; Fuller et al., 2014; Harrison et al., 2013; Healy et al., 2017; Zotter et al., 2017; Helin et al., 2018)

The interpretation of α_{abs} is ambiguous since it not only depends on the dominant absorber but also on the size and internal structure of the particles, core size and shell thickness. For instance, for pure BC particles, α_{abs} may be < 1 and BC particles coated with non-absorbing material may have α_{abs} in the range from <1 to ~ 1.7 (e.g., Gyawali et al., 2009; Lack and Cappa, 2010; Lack and Langridge, 2013; Schuster et al., 2016; Liu et al., 2018; Chylek et al., 2019; Zhang et al., 2020). The present paper may be considered as an extension to the above-mentioned analyses since they did not explicitly analyze the effects on the Aethalometer model.

The aim of this study is to estimate uncertainties of the Aethalometer-model-derived fractions of absorption by eBC from fossil fuel and biomass burning when spherical BC cores are coated by some non-absorbing material. To state this more clearly, it is assumed that there is only one type of BC particles that can be called fossil fuel BC in the Aethalometer model terminology. Consequently, any deviations from biomass-burning fraction of $BB\% = 0$ indicate uncertainty in the source appointment. Biomass-burning fractions were calculated for pure and coated single particles, for lognormal unimodal and bimodal size distributions. The work is based on modeling only, no measurement data are used.

2. Methods

The BC cores were assumed to be coated with an ammonium sulfate shell by using two approaches. It was assumed 1) that the shell thickness the same for all particles in a size distribution (Fig. 1a) and 2) that the core volume fraction is the same for all particles in a size distribution (Fig. 1b). The core volume fraction was calculated from

$$f_c = \frac{V_{core}}{V_p} = \left(\frac{D_{core}}{D_p} \right)^3 = \left(\frac{D_{core}}{D_{core} + 2s} \right)^3 \quad (1)$$

where V_p is the particle volume, V_{core} is the BC core volume, D_p is the particle diameter ($= D_{core} + 2s$), D_{core} is the BC core diameter and s the shell thickness. The shell volume fraction was then calculated from $f_s = 1 - f_c$. The ratio of the coated particle diameter to the core diameter is an often used metric for presenting the coating of particles. R , f_c and f_s can be calculated from each other as

$$R = \frac{D_p}{D_{core}} = \left(\frac{1}{f_c} \right)^{1/3} = \left(\frac{1}{1 - f_s} \right)^{1/3} \quad (2)$$

The number-weighted D_p -to- D_{core} ratio is calculated from

$$R_{N(D_p)} = \frac{\sum N_i R_i}{N_{tot}} = \frac{\sum N_i (D_{p,i} / D_{core,i})}{N_{tot}} \quad (3)$$

where N_i and R_i are the number concentration and D_p -to- D_{core} ratio of the particle diameter $D_{p,i}$, respectively. If f_s is independent of particle size – which is the assumption used in some of the simulations below – equation (3) simplifies to $R_{N(D_p)} = R$.

Lognormal size distributions $n(D_p, D_g, \sigma_g)$ were generated where D_p is the particle diameter, D_g is the geometric mean diameter and σ_g the geometric standard deviation. The D_p range was 3 nm – 10 μ m. For the unimodal size distributions D_g range was 50 nm – 1 μ m and σ_g was given three values 1.4, 1.6, 1.8 (Fig. 1c and 1d). Also bimodal size distributions were generated. For the small-particle mode the geometric mean diameter D_{g1} range was 50 – 100 nm, and the large-particle mode D_{g2} range was 100 – 500 nm. In addition to varying the geometric mean diameters also the ratios of the number of particles in the two modes were varied. Two cases were used for this: 1) $N_1 = 10N_2$, $\sigma_{g1} = 1.4$, $\sigma_{g2} = 1.6$ (Fig. 1e) and 2) $N_1 = N_2$, $\sigma_{g1} = 1.6$, $\sigma_{g2} = 1.6$ (Fig. 1f).

Absorption coefficients were calculated from

$$\sigma_{ap}(\lambda) = \int Q_a(\lambda, D_p, m_{core}, m_{shell}, s) \frac{\pi}{4} D_p^2 n(D_p) dD_p \quad (4)$$

where Q_a is the absorption efficiency that is a function of the wavelength λ , D_p , the complex refractive indices of the core and shell, m_{core} and m_{shell} , respectively, and the shell thickness s . Q_a was calculated using the N-Mie Fortran code that is based on a recursive algorithm of Wu and Wang (1991). The code calculates the extinction, scattering and absorption efficiency factors for n-layered spheres. The complex refractive indices were $m_{core} = 1.85 + 0.71i$ (BC as in Lack and Cappa, 2010) and $m_{shell} = 1.52 + 0i$ (ammonium sulfate) for the core and shell, respectively. Absorption coefficients were calculated for the Aethalometer wavelengths $\lambda = 470$ nm and 950 nm and α_{abs} was calculated from

$$\alpha_{abs}(470/950) = - \frac{\ln(\sigma_{ap}(\lambda = 470nm) / \sigma_{ap}(\lambda = 950nm))}{\ln(470/950)} \quad (5)$$

The wavelengths 470 nm and 950 nm were used as they are used also in the AE33 automatic source apportionment. In analyses of aerosol optical depth data from the AERONET network α_{abs} is often

calculated for the wavelength pair 440 nm and 870 nm (Russell et al., 2010; Schuster et al., 2016). To evaluate the applicability of the simulations of the present work to AERONET data analyses σ_{ap} was calculated also for these wavelengths and the respective α_{abs} was calculated from them. There are size-dependent differences between $\alpha_{abs}(470/950)$ and $\alpha_{abs}(440/870)$ but they are not big, see the supplement, Figs. S1 and S2, so it may safely be concluded that the results to be presented below are valid also for the AERONET data.

For the absorption due to particles from wood burning or biomass burning Zotter et al. (2017) give the equation

$$\sigma_{ap,bb}(\lambda_2) = \frac{\sigma_{ap}(\lambda_1) - \sigma_{ap}(\lambda_2) \left(\frac{\lambda_1}{\lambda_2} \right)^{-\alpha_{ff}}}{\left(\frac{\lambda_1}{\lambda_2} \right)^{-\alpha_{bb}} - \left(\frac{\lambda_1}{\lambda_2} \right)^{-\alpha_{ff}}} \quad (6)$$

where α_{ff} and α_{bb} are the α_{abs} of fossil fuel and biomass burning BC in the Aethalometer model. Noting that $\sigma_{ap}(\lambda_1) = \sigma_{ap}(\lambda_2) (\lambda_1/\lambda_2)^{-\alpha_{abs}}$ the fraction of absorption due to biomass burning is

$$BB(\%) = 100\% \frac{\sigma_{ap,bb}(\lambda_2)}{\sigma_{ap}(\lambda_2)} = 100\% \frac{\left(\frac{\lambda_1}{\lambda_2} \right)^{-\alpha_{abs}} - \left(\frac{\lambda_1}{\lambda_2} \right)^{-\alpha_{ff}}}{\left(\frac{\lambda_1}{\lambda_2} \right)^{-\alpha_{bb}} - \left(\frac{\lambda_1}{\lambda_2} \right)^{-\alpha_{ff}}} \quad (7)$$

so that BB% depends on the Ångström exponents α_{abs} , α_{ff} and α_{bb} . Two settings for the constants were used, the one presented in the AE33 manual: $\alpha_{ff} = 1$ and $\alpha_{bb} = 2$, and the one presented by Zotter et al. (2017): $\alpha_{ff} = 0.9$ and $\alpha_{bb} = 1.68$.

3. Results and discussion

3.1 Single particles

The absorption Ångström exponent α_{abs} and the fraction of biomass-burning BC for single coated particles are shown in Fig. 2. The dashed lines in Figs. 2a, 2c, and 2e show the core diameter D_{core} of particles that have the same diameter D_p at all shell thicknesses. In Figs. 2b, 2d and 2f the dashed lines show the particle diameter D_p and f_s of particles that have the same D_{core} at all shell volume fractions f_s

1 in the range $f_s \leq 99\%$. The dependence of α_{abs} on core and shell is presented twice. This is apparently
2 superfluous but they are visualizations that complement each other.

3
4 The first approach (Figs. 2a, 2c, and 2e) shows that when $D_{core} < \sim 150$ nm and $s > \sim 25 - 50$ nm the
5 absorption Ångström exponent $\alpha_{abs} > 1.4$. The respective BB fractions are larger than about 40% or 60%
6 for the Aethalometer model parameters of $\alpha_{ff} = 1$, $\alpha_{bb} = 2$ (pair 1) and $\alpha_{ff} = 0.9$, $\alpha_{bb} = 1.68$ (pair 2),
7 respectively. Fig. 2a also shows that for $D_{core} < \sim 100$ nm there are two maxima of the α_{abs} when the
8 shell grows thicker. In the second maximum $\alpha_{abs} > \sim 1.6$. As a result the BB fractions would be $> 60\%$
9 and even $> 100\%$ for the two Aethalometer model parameter pairs. When D_{core} is in the range of ~ 170 -
10 200 nm $\alpha_{abs} \approx 1$ and α_{abs} decreases with a growing s . For larger core diameters the absorption Ångström
11 exponent is even smaller. When $D_{core} > 200$ nm $\alpha_{abs} < 1$, and even negative for $D_{core} > \sim 360$ nm. Further,
12 when $D_{core} > 200$ nm, α_{abs} does not grow essentially at all as a function of s .

13
14 The visualization of α_{abs} as a function of shell volume fraction f_s and particle full diameter D_p (Fig. 2b)
15 shows some other features. When $D_p < 50$ nm, α_{abs} varies in the range of 1.0 - 1.1 and it does not depend
16 on f_s but in the D_p range of about 100 – 300 nm α_{abs} depends strongly on f_s . When $D_p \approx 500$ nm $\alpha_{abs} <$
17 1 for almost all shell volume fractions, up to $f_s \sim 99\%$. For larger particles α_{abs} is close to 0 at all shell
18 volume fractions.

19
20 The visualization also shows that the α_{abs} value of 1, usually considered as indication of BC, is not a
21 result of an unambiguous D_{core} - s (Fig. 2a) or D_p - f_s (Fig. 2b) combination.

22 23 **3.2 Unimodal BC core size distributions, same coating thickness for all sizes**

24 For single particles α_{abs} depends clearly both the core size and the shell thickness. However, in real
25 atmospheric studies the wavelength dependency of absorption by particle size distributions are
26 measured. Here these were first modeled by assuming that pure BC particle size distributions get
27 coated with ammonium sulphate layers so that the shell thickness is independent of particle size as
28 visualized in Fig. 1a. For example, the shell thickness on a 50 nm BC particle would be the same as on a
29 200 nm particle which means the shell volume fractions are not the same. The BC core geometric mean

diameter ($D_{g,core}$) was varied from 50 to 200 nm at 10 nm intervals. The geometric standard deviations of the size distributions were $\sigma_g = 1.4$, $\sigma_g = 1.6$, and $\sigma_g = 1.8$ representing narrow, average and wide size distributions. The shell thickness s varied from 0 to 250 nm at 1 nm intervals. Absorption coefficient and subsequently α_{abs} was calculated for the full size distribution 3 – 2500 nm.

The results are first shown as a function of $D_{g,core}$ and shell thickness s for the three size distribution widths (Fig. 3). There are both similarities and differences compared with the corresponding relationships of single particles (Fig. 2). For example, for single particles $\alpha_{abs} \approx 1$ at $D_{core} \approx 180$ nm for shell thicknesses $s \approx 0 - 70$ nm as shown by the almost vertical $\alpha_{abs} = 1$ isoline in Fig. 2a whereas for the size distributions with $\sigma_{g,core} > 1$ the respective isoline is a strong function of both s and $\sigma_{g,core}$ (Fig. 3a). At all widths of the size distribution α_{abs} increases with increasing shell thickness and then starts decreasing. For small core sizes ($D_{g,core} < \sim 80$ nm) α_{abs} has also a second maximum when the size distribution is narrow. The width of the size distribution has a clear effect on the α_{abs} : for all core sizes and shell thicknesses α_{abs} decreases with increasing $\sigma_{g,core}$.

Both for single particles and size distributions the first maximum of α_{abs} is the smaller the larger the $D_{g,core}$ and $\sigma_{g,core}$ are (Fig. 4a). The first maximum is reached at shell thickness $s \approx 70 \pm 5$ nm for all size distribution widths although for single particles the variability of the shell thickness corresponding to the first maximum is larger (Fig. 4b). The first maximum α_{abs} results in apparent BB fractions of up to $\sim 100\%$ for single particles and in the range from 0 to $\sim 80\%$ for the size distributions and again the BB(%) is the smaller the larger the $D_{g,core}$ and σ_g are (Fig. 4c and d).

This approach is further followed by plotting the parameters as a function of shell thickness for three different BC core diameters, 50 nm, 70 nm, and 90 nm of single particles and core size distributions with the geometric standard deviations of $\sigma_{g,core} = 1.4$, 1.6, and 1.8 (Fig. 5). This analysis can be considered as a description of what may happen to the size distribution, α_{abs} and the apparent BB(%) during condensational growth on fresh small BC cores if the growing shell thickness were independent of the core diameter, even if this is unrealistic. The shell volume fraction f_s increases to $> 99.9\%$ when the shell thickness grows from $s = 0$ nm to 250 nm on single 50 nm particles but to lower fractions for

the wider size distributions and larger core sizes so that for $D_{g,core} = 90$ nm and $\sigma_g = 1.8$ $f_s \approx 98\%$ even with $s = 250$ nm (Fig. 5a). The geometric mean diameter D_g of the whole size distribution grows to ~ 600 nm when the shell thickness grows to 250 nm, minimal differences between the original widths (Fig. 5b). The width of the size distribution, i.e., σ_g decreases fast to < 1.2 (Fig. 4c). Such values correspond to very narrow size distributions, not really observed in the real atmosphere.

The number-weighted D_p -to- D_{core} ratio $R_{N(Dp)}$, Eq. (3), was calculated for the size range 90-600 nm to present the numbers comparable with papers that present shell-to-core ratios of refractory BC (rBC) obtained from SP2 measurements. For instance, Kondo et al. (2011) measured urban air of Tokyo and obtained the median $R = 1.1$ with a range up to about 1.3, the mean $D_g = 64 \pm 6$ nm, and $\sigma_g = 1.66 \pm 0.12$. Moteki et al. (2007) conducted SP2 measurements in an aircraft in urban plumes on the Japanese coast. They fitted the data with lognormal size distributions with mass median diameters (MMD) of 190 and 210 nm and σ_g of 1.55 and 1.45 for fresh and aged rBC, respectively. The fresh rBC was thinly coated with $R < 2$ and the aged rBC thickly coated with $R \sim 2$. The MMD and σ_g values yield $D_g = 107$ nm and 139 nm. Shiraiwa et al. (2008) measured the mixing state and size distribution of BC aerosol with an SP2 at a remote island (Fukue) in Japan. They observed that the BC number median diameters were in the range of 120–140 nm in every air mass type and the median shell/core diameter ratio (R) in different air masses varied in the range of 1.2 – 1.6. However, they also observed that the fraction of R values in the range 2 – 3.5 was not negligible either (Fig. 9 of Shiraiwa et al., 2008). Such values correspond to the range where α_{abs} first grows to >1.6 for the narrow ($\sigma_{g,core} = 1.4$) BC core size distribution that has the smallest geometric mean size ($D_{g,core} = 50$ nm) but to lower values for the wider size distributions that have larger $D_{g,core}$ (Fig. 5c and 5d). The first maximum is reached at shell thicknesses of $s \approx 70$ nm that corresponds to $R \approx 2$ and shell volume fractions of $f_s \approx 90 \pm 8\%$ (Fig. 5b). Schwarz et al. (2008) reported statistics of rBC mass size distributions in urban aerosol: $f_s = 9 \pm 6\%$, $s = 20 \pm 10$ nm, MMD = 170 nm, and σ_g of 1.71 which yields $D_g = 72$ nm; in biomass burning emissions: $f_s = 70 \pm 9\%$, $s = 65 \pm 12$ nm, MMD = 210 nm, $\sigma_g = 1.43$ which yields $D_g = 143$ nm and in background continental aerosol: $f_s = 46 \pm 3\%$, $s = 48 \pm 14$ nm, MMD = 210 nm, 1.55 which yields $D_g = 118$ nm.

1 The referenced studies show that the s , R , and f_s values are in the range observed in ambient
2 measurements studies. What is not realistic in atmospheric aerosol is the width of the size distribution,
3 which soon decreases to $\sigma_g < 1.2$ (Fig. 5c).

4
5 After reaching the first maximum α_{abs} decreases and for single particles and the narrowest core size
6 distributions starts again growing and reaches a second maximum at shell thicknesses of $s \approx 170$ nm
7 that corresponds to $R > 4$ and $f_s > 98\%$. Such s and R values are not in the range observed in the above-
8 mentioned studies, nor are the low geometric standard deviations of $\sigma_g < 1.1$ realistic so the second
9 maximum can be considered as a theoretical value only. For size distributions with $D_{g,core} > 70$ nm there
10 is no second maximum of α_{abs} .

11
12 As α_{abs} increases and decreases it is clear that this applies to BB(%) as well (Fig. 5d-e). For the smallest
13 core sizes ($D_{g,core} = 50$ nm) and the narrowest size distributions ($\sigma_{g,core} = 1.4$) the first maximum BB(%)
14 may be as high as ~90% when the values of $\alpha_{ff} = 0.9$, $\alpha_{bb} = 1.68$ are used in Eq. (7) but lower, ~50%
15 when the values of $\alpha_{ff} = 1$, $\alpha_{bb} = 2$ are used. For the wider core size distributions the BB(%) fractions are
16 lower. For the widest core size distributions ($\sigma_{g,core} = 1.8$) clearly positive BB(%) values are reached only
17 for the smallest core sizes.

18
19 Fig. 5 can also be considered as a proxy for a time series of the development of α_{abs} and derived BB(%)
20 after emission of BC particles and their growth by condensation of nonabsorbing compounds. Similar
21 development – α_{abs} increase to > 1.3 and decrease to < 0.9 during a several-day-long pollution episode
22 during which the D_g of the whole size distribution grew possibly by condensation – was observed at
23 SORPES in Nanjing, China (Fig. 9 of Shen et al., 2018). There was no SP2 available for the core-shell
24 structure measurements in that study so it cannot really be proven that the observed α_{abs} development
25 was due to condensational growth even though it seems a good explanation and is qualitatively in line
26 with Fig. 5.

3.3 Unimodal size distributions with the same BC core fraction for all sizes

The second approach is to assume that the BC core fraction – or equivalently the shell volume fraction – is the same for all sizes which means that the shell thickness increases with size as was visualized in Fig. 1b. This can be considered to be a result of aging of BC by not only condensational growth but also by cloud processing. The latter would lead to thick shells on particles activated into cloud droplets that would absorb for instance SO_2 and NH_3 and that would not rain but get later back into the aerosol phase by evaporation of cloud water. The constant volume fraction is not realistic but neither is the constant shell thickness. Both can be considered to be approximations.

In this approach the geometric standard deviations of the whole size distributions were set to $\sigma_g = 1.4$, 1.6 and 1.8 and the shell volume fractions f_s to vary from 0% to 99%. The resulting α_{abs} and BB(%) are presented as a function of D_g , f_s and σ_g (Fig. 6). They are comparable with the analogous plots for single particles, i.e., $\sigma_g = 1.0$ (Fig. 2b, 2d, and 2f). Note that from Eq. (2) it follows that the assumption of a constant f_s means that also the D_p -to- D_{core} ratio R is constant and that the f_s range of 0 to 99% corresponds to the R range of 1 to 4.6. Figure 6 therefore has two y axes, one showing the f_s and the other the corresponding R values.

Several observations can be made from Fig. 6. One of them is that the isoline of $\alpha_{\text{abs}} = 1$ grows with growing D_g for each of the size distribution widths (σ_g) but decreases with growing σ_g . Another is that the wider the size distribution is, the lower are the α_{abs} and BB(%) at any given shell volume fraction. The third one is that for all three widths α_{abs} and BB(%) grows when f_s grows but that the growth is not uniformly distributed over the f_s vs. D_g space.

The last observation leads to calculations of size-dependent sensitivities of α_{abs} to variations in f_s . The sensitivity was calculated as $d\alpha_{\text{abs}}/df_s$ and its unit is $\%^{-1}$. Fig. 7a shows the sensitivities in the whole f_s range of 1 - 99% as a function of D_g for the three size distribution widths. The sensitivity depends clearly on both D_g and σ_g of the size distribution and it also varies with f_s . It is very clear that α_{abs} is most sensitive to f_s variations when D_g of the size distribution is in the accumulation mode sizes of 100 – 200

nm. The sensitivity grows fairly steadily with growing f_s until for $f_s > 90\%$ – which equals $R > 2$ – it increases very strongly.

Another step for visualizing the sensitivities was taken by calculating size-dependent average sensitivities of α_{abs} and $BB(\%)$ in three f_s ranges: $f_s = 0 - 50\%$, $50 - 90\%$ and $90 - 99\%$ (Fig. 7b and 7c).

According to Eq. (2) the f_s ranges correspond to the R ranges of $1 - 1.3$, $1.3 - 2.2$ and $2.2 - 4.6$. The lines in Fig. 7b and 7c can be used for a rough estimate on a possible effect on α_{abs} and $BB(\%)$. For instance, if $D_g \approx 140$ nm, $\sigma_g = 1.4$, and $f_s \approx 50 - 90\%$, an increase of f_s from 50% to 51% leads to an α_{abs} increase of ~ 0.01 and consequently to a $BB(\%)$ increase of $\sim 1\%$ when Aethalometer model constants of $\alpha_{ff} = 0.9$, $\alpha_{bb} = 1.68$ are used.

3.4 Bimodal size distributions with the same BC core fraction for all sizes in the mode

Finally, bimodal size distributions are examined briefly. The size distributions consist of two externally mixed modes that have different shell volume fractions. In both modes the shell volume fractions are size-independent as in Fig. 1b. Mode 1 is an Aitken mode with the geometric mean diameter D_{g1} in the range $50 - 100$ nm. There are two different settings for the Aitken mode: in the first case its number concentration is 10 times larger than that of the accumulation mode, i.e., $N_1 = 10N_2$, it consists of almost pure fresh BC particles with $f_{s1} = 5\%$ ($R \approx 1.02$) and it is narrow, $\sigma_{g1} = 1.4$. In the second setting the number concentrations of the Aitken and accumulation mode are equal ($N_1 = N_2$), the Aitken mode is aged so that $f_{s1} = 50\%$ ($R \approx 1.3$) and it is wider, $\sigma_{g1} = 1.6$. Mode 2 is an accumulation mode with the geometric mean diameter D_{g2} in the range $100 - 500$ nm, $\sigma_{g2} = 1.6$ and it is very aged, with $f_{s2} = 98\%$ ($R \approx 3.7$). The accumulation mode could be the result of cloud processing as explained above.

The results show that α_{abs} is more sensitive to variations of the accumulation mode than of the Aitken mode (Fig. 8a). For instance, if $D_{g2} < 250$ nm, $\alpha_{abs} > 1$ at all D_{g1} values. Also, if $D_{g1} = 60$ nm and D_{g2} varies in the whole range of $100 - 500$ nm, α_{abs} varies in the range of $\sim 0.4 - 1.3$. When the Aitken mode dominates the number concentration ($N_1 = 10N_2$) with the fresh BC particles the maximum $\alpha_{abs} \approx 1.2$ at $D_{g1} \approx 60$ nm and $D_{g2} \approx 140$ nm is smaller than when the two modes have equal amount of particles. In the latter case the maximum $\alpha_{abs} > 1.3$. When the Aitken mode with $f_s = 5\%$ dominates the number

concentration the whole size distribution moves to the region that is less sensitive to f_s variations as discussed above in section 3.3. It is worth noting also that the maximum α_{abs} and BB(%) values (Fig. 8b and 8c) are smaller than derived from the unimodal size distributions (section 3.3).

4. Summary and conclusions

The purpose of this study is not to claim that all Aethalometer model results are wrong but that they have higher uncertainties than have been discussed in the literature. It is clear that there are BrC particles that have absorption Ångström exponents clearly larger than one, as shown in a very large number of publications. However, the size of light-absorbing particles and their coating even by purely scattering material affect clearly the wavelength dependence of absorption and thus have the potential to affect the Aethalometer model results. Since the wavelength dependency is used for source apportionment these effects have the potential to result in tens of percent too high or low contributions of wood-burning or fossil fuel emissions.

There are some important results. In the modeling α_{abs} equals 1 or 0.9 in very rare cases and thus BB(%) was very seldom 0% even though one type of BC was the only absorbing material in the simulations. The shape of size distribution plays an important role. Narrow size distributions result in higher α_{abs} and BB(%) values than wide size distributions. The sensitivity of α_{abs} and BB(%) to variations in shell volume fractions is the highest for accumulation mode particles. This is important because that is where the largest aerosol mass is.

The goal of the paper was not to find out whether some pair of α_{ff} and α_{bb} is better than the other. Two well-known α_{ff} and α_{bb} pairs were used and shown how large the uncertainties may become just for these two pairs even if BC particles were coated by purely scattering material. The goal was not at all to find a good pair. On the contrary, the study shows that no constant values are good since in the real atmosphere BC particle size distributions are not constant, neither their mean diameter nor the coating of the particles. They all vary dynamically in the atmosphere. The study shows that any constant values will undoubtedly lead to large uncertainties of both the BB and FF fractions if no information on the size of the core or the thickness of the shell is available, even if purely scattering material is coating BC

cores. As a conclusion, for the interpretation of absorption Ångström exponents it would be very important to measure BC size distributions and shell thicknesses together with the wavelength dependency of absorption.

There are obvious limitations in this study. A core-shell Mie model was used only so the work is limited to spherical particles. Fresh BC particles are usually agglomerates. There are studies that show that during aging processes these agglomerates may collapse and become closer to spherical particles so Mie modeling probably agrees better for aged than fresh BC particles. Further, even if particles were spherical how well can they be modeled with a Mie code when they are collected on filters? Or does light absorption then follow the spectral absorbance of the bulk materials?

This question could in principle be answered by generating spherical BC particles, coating them in an aging chamber with some non-absorbing material, for instance ammonium sulfate, and measuring both light absorption at multiple wavelengths with an Aethalometer and BC core size distributions and shell thicknesses with an SP2. If α_{abs} increases up to some maximum value as a function of shell thickness and then starts decreasing like in the simulations above, then the process agrees with the growth of a size-independent coating. Or if α_{abs} increases steadily then it suggests that the growth is size-dependent and possibly with a size-independent shell volume fraction growth rate. If these are observed then the uncertainties discussed in this work should be taken seriously.

On the other hand, if none of these effects were observed and the absorption Ångström exponents of the collected particles were ≈ 1 regardless of core size and shell thickness it would be safe to say that the Aethalometer measures the absorption spectra of the bulk materials and that the Aethalometer model yields correct results. Probably the truth is somewhere between these extremes: when the filter tape is still relatively clean the particles can be modeled even with a Mie code and for heavily-loaded filters α_{abs} is that of bulk material. Also this could and should be tested experimentally.

Acknowledgements This work was supported by the Academy of Finland via project NABCEA (grant no. 296302) and by Business Finland via project BC Footprint (grant nr. 528/31/2019).

References

- Andreae, A. and Gelencser, A.: Black carbon or brown carbon? The nature of light-absorbing carbonaceous aerosols, *Atmos. Chem. Phys.*, 6, 3131–3148, <http://www.atmos-chem-phys.net/6/3131/2006>, 2006.
- Arola, A., Schuster, G., Myhre, G., Kazadzis, S., Dey, S., and Tripathi, S. N.: Inferring absorbing organic carbon content from AERONET data, *Atmos. Chem. Phys.*, 11, 215–225, <https://doi.org/10.5194/acp-11-215-2011>, 2011.
- Bergstrom, R.W., Pilewskie, P., Russell, P. B., Redemann, J., Bond, T., Quinn, P. K., and Sierau, B.: Spectral Absorption Properties of Atmospheric Aerosols, *Atmos. Chem. Phys.*, 7, 5937–5943, <http://www.atmos-chem-phys.net/7/5937/2007>, 2007.
- Bond, T. C. and Bergstrom, R. W.: Light Absorption by Carbonaceous Particles: An Investigative Review, *Aerosol Sci. Technol.*, 40, 27–67, 2006.
- Bond, T. C., Doherty, S. J., Fahey, D. W., Forster, P. M., Berntsen, T., DeAngelo, B. J., Flanner, M. G., Ghan, S., Kärcher, B., Koch, D., Kinne, S., Kondo, Y., Quinn, P. K., Sarofim, M. C., Schultz, M. G., Schulz, M., Venkataraman, C., Zhang, H., Zhang, S., Bellouin, N., Guttikunda, S. K., Hopke, P. K., Jacobson, M. Z., Kaiser, J. W., Klimont, Z., Lohmann, U., Schwarz, J. P., Shindell, D., Storelvmo, T., Warren, S. G., and Zender, C.S.: Bounding the role of black carbon in the climate system: A scientific assessment, *J. Geophys. Res. Atmos.*, 118, 2013.
- Cazorla, A., Bahadur, R., Suski, K. J., Cahill, J. F., Chand, D., Schmid, B., Ramanathan, V., and Prather, K. A.: Relating aerosol absorption due to soot, organic carbon, and dust to emission sources determined from in-situ chemical measurements, *Atmos. Chem. Phys.*, 13, 9337–9350, <https://doi.org/10.5194/acp-13-9337-2013>, 2013.

1 Chung, C., Ramanathan, V., and Decremmer, D.: Observationally constrained estimates of carbonaceous
2 aerosol radiative forcing, *P. Natl. Acad. Sci. USA*, 109, 11624–11629, 2012.

3
4 Chylek, P., Lee, J. E., Romonosky, D. E., Gallo, F., Lou, S., Shrivastava, M., et al.: Mie scattering captures
5 observed optical properties of ambient biomass burning plumes assuming uniform black, brown, and
6 organic carbon mixtures. *J. Geophys. Res., Atmospheres*, 124, 11406–11427.
7 <https://doi.org/10.1029/2019JD031224>, 2019.

8
9 Devi, J.J., Bergin, M., McKenzie, M., Schauer, J.J., and Weber, R.: Contribution of particulate brown
10 carbon to light absorption in the rural and urban Southeast US, *Atmos. Environ.*, 136, 95 - 104, 2016.

11
12 Feng, Y., Ramanathan, V., and Kotamarthi, V. R.: Brown carbon: a significant atmospheric absorber of
13 solar radiation?, *Atmos. Chem. Phys.*, 13, 8607–8621, <https://doi.org/10.5194/acp-13-8607-2013>,
14 2013.

15
16 Fuller, G.W., Tremper, A.H., Baker, T.D., Yttri, K.E., Butterfield, D.: Contribution of wood burning to
17 PM₁₀ in London. *Atmos. Environ.* 87, 87–94, 2014.

18
19 Gyawali, M., Arnott, W. P., Lewis, K., and Moosmüller, H.: In situ aerosol optics in Reno, NV, USA during
20 and after the summer 2008 California wildfires and the influence of absorbing and non-absorbing
21 organic coatings on spectral light absorption, *Atmos. Chem. Phys.*, 9, 8007-8015, doi:10.5194/acp-9-
22 8007-2009, 2009.

23
24 Harrison, R.M., Beddows, D.C., Jones, A.M., Calvo, A., Alves, C., Pio, C.: An evaluation of some issues
25 regarding the use of aethalometers to measure woodsmoke concentrations. *Atmos. Environ.* 80, 540–
26 548, 2013.

1 Healy, R., Sofowote, U., Su, Y., Debosz, J., Noble, M., Jeong, C.-H., Wang, J., Hilker, N., Evans, G.,
2 Doerksen, G.: Ambient measurements and source apportionment of fossil fuel and biomass burning
3 black carbon in Ontario. *Atmos. Environ.* 161, 34–47, 2017.

4

5 Helin, A., Niemi, J., Virkkula, A., Pirjola, L., Teinilä, K., Backman, J., Aurela, M., Saarikoski, S., Rönkkö, T.,
6 Asmi, E., Timonen, H.: Characteristics and source apportionment of black carbon in the Helsinki
7 metropolitan area, Finland, *Atmos. Environ.*, 190, 87 – 98, doi: 10.1016/j.atmosenv.2018.07.022, 2018.

8

9 Herich, H., Hueglin, C., and Buchmann, B.: A 2.5 year's source apportionment study of black carbon
10 from wood burning and fossil fuel combustion at urban and rural sites in Switzerland, *Atmos. Meas.*
11 *Tech.*, 4, 1409–1420, doi:10.5194/amt-4-1409-2011, 2011.

12

13 Kirchstetter, T. W., Novakov, T., and Hobbs, P. V.: Evidence that the spectral dependence of
14 light absorption by aerosols is affected by organic carbon, *J. Geophys. Res.*, 109, D21208,
15 doi:10.1029/2004JD004999, 2004.

16

17 Kirchstetter, T. W. and Thatcher, T. L.: Contribution of organic carbon to wood smoke particulate matter
18 absorption of solar radiation, *Atmos. Chem. Phys.*, 12, 6067–6072, doi:10.5194/acp-12-6067-2012,
19 2012.

20

21 Kondo, Y., L. Sahu, N. Moteki, F. Khan, N. Takegawa, X. Liu, M. Koike, and T. Miyakawa: Consistency and
22 traceability of black carbon measurements made by laser-induced incandescence, thermal-optical
23 transmittance, and filter-based photo-absorption techniques, *Aerosol Sci. Technol.*, 45, 295–312,
24 doi:10.1080/02786826.2010.533215, 2011.

25

26 Lack, D. A. and Cappa, C. D.: Impact of brown and clear carbon on light absorption enhancement,
27 single scatter albedo and absorption wavelength dependence of black carbon, *Atmos. Chem. Phys.*,
28 10, 4207-4220, doi:10.5194/acp-10-4207-2010, 2010.

Lack, D. A. and Langridge, J. M.: On the attribution of black and brown carbon light absorption using the Ångström exponent, *Atmos. Chem. Phys.*, 13, 10535-10543, <https://doi.org/10.5194/acp-13-10535-2013>, 2013.

Lack, D. A., Langridge, J. M., Bahreini, R., Cappa, C. D., Middlebrook, A. M., and Schwarz, J. P.: Brown carbon and internal mixing in biomass burning particles, *P. Natl. Acad. Sci. USA*, 109, 14802–14807, 2012.

Laskin, A., Laskin, J., and Nizkorodov, S. A.: Chemistry of Atmospheric Brown Carbon, *Chem. Rev.*, 115, 4335–4382, <https://doi.org/10.1021/cr5006167>, 2015.

Liu, C., Chung, C. E., Yin, Y., and Schnaiter, M.: The absorption Ångström exponent of black carbon: from numerical aspects, *Atmos. Chem. Phys.*, 18, 6259-6273, <https://doi.org/10.5194/acp-18-6259-2018>, 2018.

Moosmüller, H., Chakrabarty, R. K., Ehlers, K. M., and Arnott, W. P.: Absorption Ångström coefficient, brown carbon, and aerosols: basic concepts, bulk matter, and spherical particles, *Atmos. Chem. Phys.*, 11, 1217–1225, [doi:10.5194/acp-11-1217-2011](https://doi.org/10.5194/acp-11-1217-2011), 2011.

Moteki, N., Y. Kondo, Y. Miyazaki, N. Takegawa, Y. Komazaki, G. Kurata, T. Shirai, D. R. Blake, T. Miyakawa, and Koike, M.: Evolution of mixing state of black carbon particles: Aircraft measurements over the western Pacific in March 2004, *Geophys. Res. Lett.*, 34, L11803, [doi:10.1029/2006GL028943](https://doi.org/10.1029/2006GL028943), 2007.

Russell, P., Bergstrom, R., Shinozuka, Y., Clarke, A., Decarlo, P., Jimenez, J., Livingston, J., Redemann, J., Dubovik, O., and Strawa, A.: Absorption Angstrom Exponent in AERONET and related data as an indicator of aerosol composition, *Atmos. Chem. Phys.*, 10, 1155-1169, 2010.

1 Saleh, R., Hennigan, C., McMeeking, G., Chuang, W., Robinson, E., Coe, H., Donahue, N., Robinson, A.:
2 Absorptivity of brown carbon in fresh and photo-chemically aged biomass-burning emissions. *Atmos.*
3 *Chem. Phys.* 13, 7683–7693, 2013.

4

5 Sandradewi, J., Prevot, A. S. H., Szidat, S., Perron, N., Alfarra, M. R., Lanz, V. A., Weingartner, E., and
6 Baltensperger, U.: Using aerosol light absorption measurements for the quantitative determination of
7 wood burning and traffic emission contributions to particulate matter, *Environ. Sci. Technol.*, 42, 3316–
8 3323, 2008a.

9

10 Sandradewi, J., Prevot, A. S. H., Weingartner, E., Schmidhauser, R., Gysel, M., and Baltensperger, U.:
11 A study of wood burning and traffic aerosols in an Alpine valley using a multi-wavelength Aethalometer,
12 *Atmos. Environ.*, 42, 101–112, 2008b.

13

14 Schuster, G. L., Dubovik, O., Arola, A., Eck, T. F., and Holben, B. N.: Remote sensing of soot carbon – Part
15 2: Understanding the absorption Ångström exponent, *Atmos. Chem. Phys.*, 16, 1587–1602,
16 <https://doi.org/10.5194/acp-16-1587-2016>, 2016.

17

18 Schwarz, J. P., Gao, R. S., Spackman, J. R., Watts, L. A., Thomson, D. S., Fahey, D. W., Ryerson, T. B.,
19 Peischl, J., Holloway, J. S., Trainer, M., Frost, G. J., Baynard, T., Lack, D. A., de Gouw, J. A., Warneke,
20 C., and Del Negro, L. A.: Measurement of the mixing state, mass, and optical size of individual black
21 carbon particles in urban and biomass burning emissions, *Geophys. Res. Lett.*, 35, L13810,
22 [doi:10.1029/2008GL033968](https://doi.org/10.1029/2008GL033968), 2008.

23

24 Shen, Y., Virkkula, A., Ding, A., Wang, J., Chi, X., Nie, W., Qi, X., Huang, X., Liu, Q., Zheng, L., Xu, Z., Petäjä,
25 T., Aalto, P. P., Fu, C., and Kulmala, M.: Aerosol optical properties at SORPES in Nanjing, east China,
26 *Atmos. Chem. Phys.*, 18, 5265–5292, <https://doi.org/10.5194/acp-18-5265-2018>, 2018.

27

Shiraiwa, M., Y. Kondo, N. Moteki, N. Takegawa, L. K. Sahu, A. Takami, S. Hatakeyama, S. Yonemura, and D. R. Blake: Radiative impact of mixing state of black carbon aerosol in Asian outflow, *J. Geophys. Res.*, 113, D24210, doi:10.1029/2008JD010546, 2008.

Valenzuela, A., Olmo, F.J., Lyamani, H., Antón, M., Titos, G., Cazorla, A., Alados-Arboledas, L.: Aerosol scattering and absorption Angström exponents as indicators of dust and dust-free days over Granada (Spain). *Atmos Res.*, 154, pp. 1-13. 2015.

Wang, X., Heald, C. L., Sedlacek, A. J., de Sá, S. S., Martin, S. T., Alexander, M. L., Watson, T. B., Aiken, A. C., Springston, S. R., and Artaxo, P.: Deriving brown carbon from multiwavelength absorption measurements: method and application to AERONET and Aethalometer observations, *Atmos. Chem. Phys.*, 16, 12733–12752, <https://doi.org/10.5194/acp-16-12733-2016>, 2016.

Wu Z.P., Wang Y.P.: Electromagnetic scattering for multilayered spheres: recursive algorithms, *Radio Science*, 26, 1393-1401, 1991.

Zhang, X., Mao, M., Yin, Y., and Tang, S.: The absorption Ångström exponent of black carbon with brown coatings: effects of aerosol microphysics and parameterization, *Atmos. Chem. Phys.*, 20, 9701–9711, <https://doi.org/10.5194/acp-20-9701-2020>, 2020.

Zotter, P., Herich, H., Gysel, M., El-Haddad, I., Zhang, Y., Močnik, G., Hüglin, C., Baltensperger, U., Szidat, S., and Prévôt, A. S. H.: Evaluation of the absorption Ångström exponents for traffic and wood burning in the Aethalometer-based source apportionment using radiocarbon measurements of ambient aerosol, *Atmos. Chem. Phys.*, 17, 4229-4249, <https://doi.org/10.5194/acp-17-4229-2017>, 2017.

1 Tables

2

3 Table 1. Nomenclature

Symbol	Definition	Unit	Equation
D_p	Particle diameter	nm	(1)
D_{core}	Diameter of the BC core particle	nm	(1)
D_g	Geometric mean diameter of a size distribution	nm	
$D_{g,core}$	Geometric mean diameter of the BC core size distribution	nm	
D_{g1}	D_g of the first mode of a bimodal size distribution	nm	
D_{g2}	D_g of the second mode of a bimodal size distribution	nm	
σ_g	Geometric standard deviation of a size distribution	-	
$\sigma_{g,core}$	Geometric standard deviation of the BC core size distribution	-	
σ_{g1}	σ_g of the first mode of a bimodal size distribution	-	
σ_{g2}	σ_g of the second mode of a bimodal size distribution	-	
$n(D_p, D_g, \sigma_g)$	Lognormal particle number size distribution	cm^{-3}	
N_1	Number concentration of the first mode of a bimodal size distribution	cm^{-3}	
N_2	Number concentration of the second mode of a bimodal size distribution	cm^{-3}	
N_i	Number concentration of particle size $D_{p,i}$	cm^{-3}	(3)
V_p	Particle volume	m^3	(1)
V_{core}	Volume of the BC core	m^3	(1)
f_c	Core volume fraction	-	(1)
f_s	Shell volume fraction	-	
s	Shell thickness	nm	(1)
R	Ratio of the particle diameter to the BC core diameter (D_p -to- D_{core} ratio)	-	(2)
$R_{N(Dp)}$	Number-weighted D_p -to- D_{core} ratio	-	(3)
R_i	D_p -to- D_{core} ratio of the particle diameter $D_{p,i}$	-	(3)
$\sigma_{ap}(\lambda)$	Absorption coefficient at the wavelength λ	Mm^{-1}	(4)
$\sigma_{ap,bb}(\lambda)$	Absorption coefficient of particles from biomass burning at the wavelength λ	Mm^{-1}	(6)
Q_a	Absorption efficiency	-	(4)
m_{core}	Complex refractive index of the BC core	-	(4)
m_{shell}	Complex refractive index of the shell	-	(4)
α_{abs}	Absorption Ångström exponent	-	
$\alpha_{abs}(\lambda_1/\lambda_2)$	Absorption Ångström exponent for the wavelength pair λ_1, λ_2	-	(5)
α_{ff}	α_{abs} of fossil fuel BC in the Aethalometer model	-	(6)
α_{bb}	α_{abs} of biomass-burning BC in the Aethalometer model	-	(6)

4

Figures

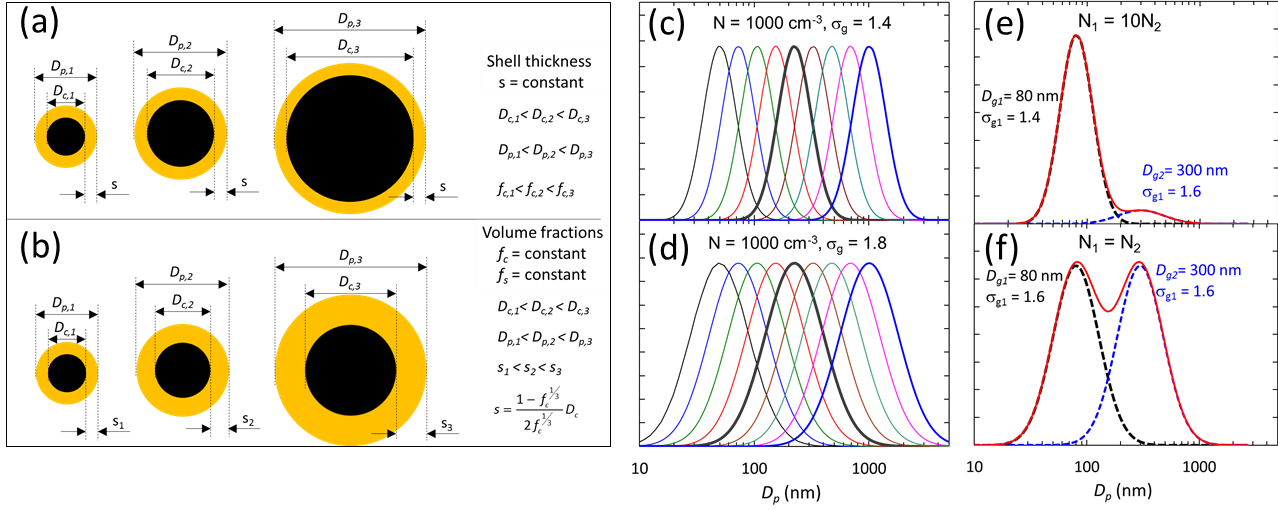


Figure 1. Examples of particles and size distributions used in the simulations: a) particles with a BC core coated with a constant shell thickness s , b) particles with constant BC core and shell volume fractions f_c and f_s , c) unimodal narrow size distributions with the geometric standard deviation of $\sigma_g = 1.4$, d) unimodal wide size distributions with $\sigma_g = 1.8$, e) bimodal size distributions with a dominating Aitken mode, f) bimodal size distributions with equal-sized Aitken and accumulation modes.

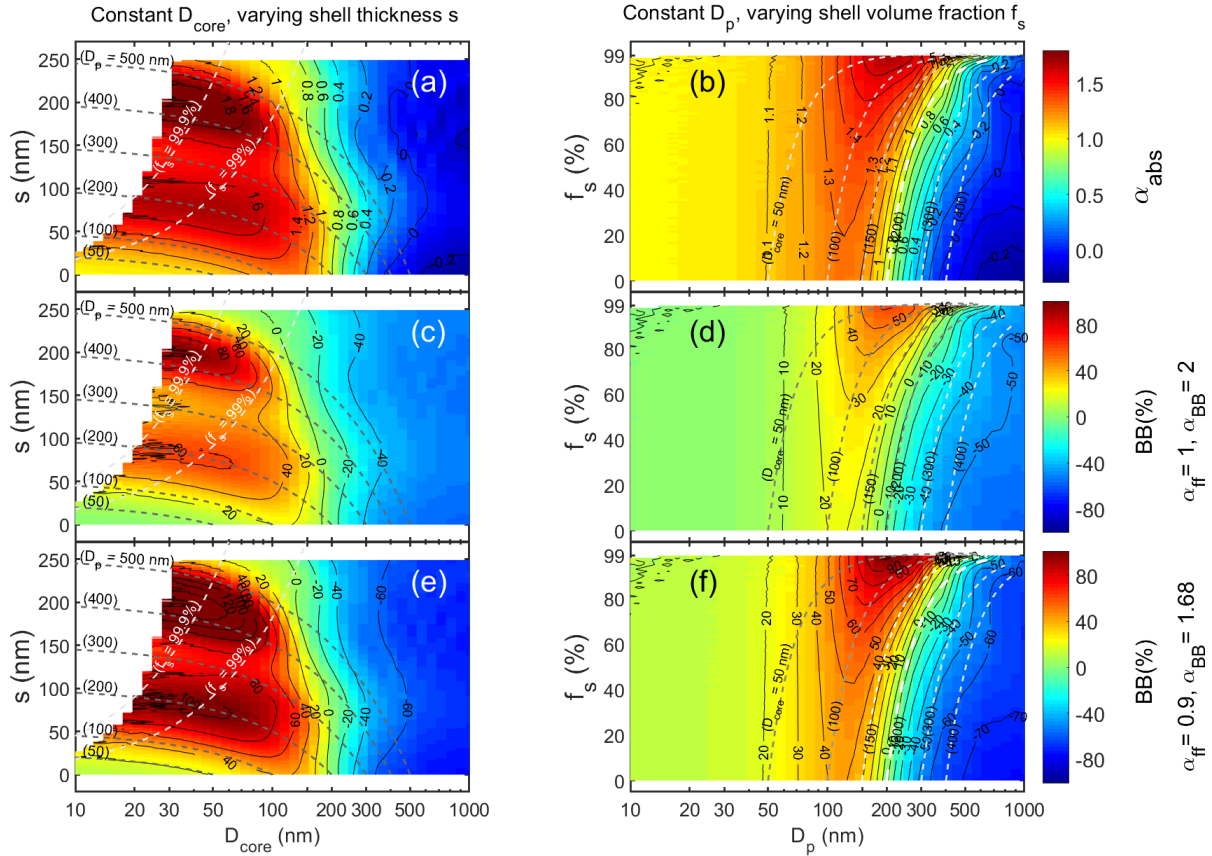
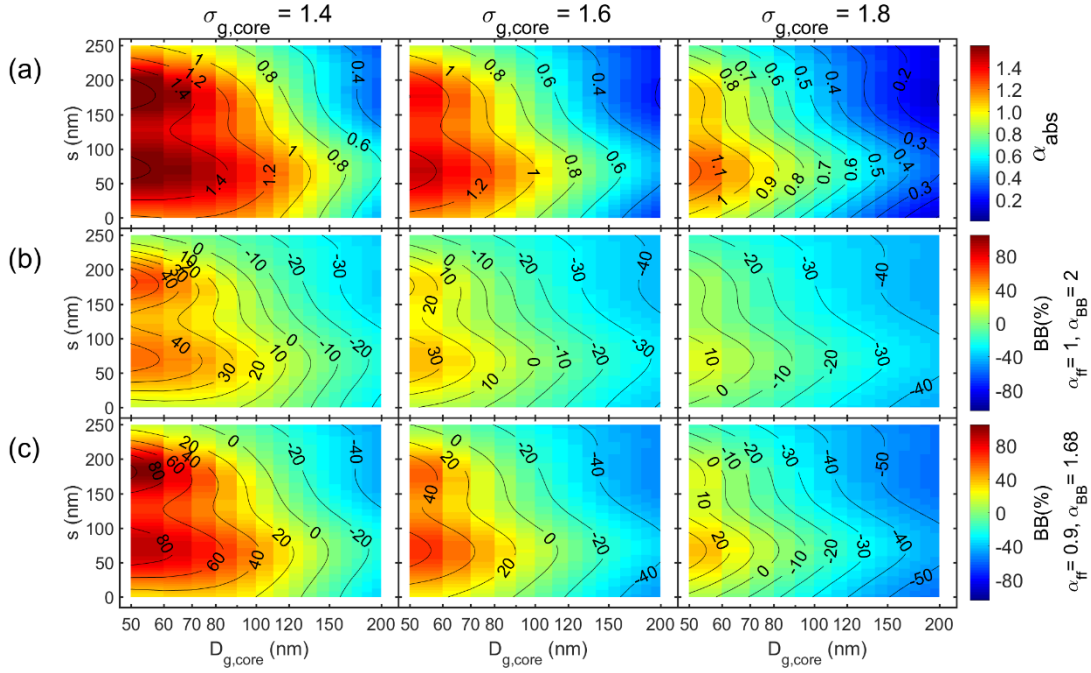


Figure 2. Absorption Ångström exponent (α_{abs}) and the from it calculated fraction of biomass-burning BC for single coated particles as a function of (in -a, c, and e) BC core diameter (D_{core}) and shell thickness (s) and (b, d, and f) as a function of particle diameter ($D_p = D_{core} + 2s$) and shell volume fraction f_s in the range $f_s \leq 99\%$. In a), c) and e) the dark dashed lines show the D_{core} and s of particles that have the same D_p – written in parentheses – at all shell thicknesses and the light dashed line show the shell thicknesses that correspond to $f_s = 99\%$ and 99.9% . In b), d) and f) the dashed lines show the D_p and f_s of particles that have the same D_{core} – written in parentheses – at all shell volume fractions. The color bars are common for a and b, c and d, and e and f.



1

2 Figure 3. Unimodal particle size distributions with a size-independent shell thickness (s) for three widths
 3 of the core size distributions: $\sigma_{g,core} = 1.4, 1.6$ and 1.8 . a) absorption Ångström exponent (α_{abs}) and the
 4 from it calculated fraction of biomass-burning BC (BB(%)) with the Aethalometer model constants of b)
 5 $\alpha_{ff} = 1, \alpha_{bb} = 2$ and c) $\alpha_{ff} = 0.9, \alpha_{bb} = 1.68$ vs. the geometric mean diameter of the core ($D_{g,core}$).

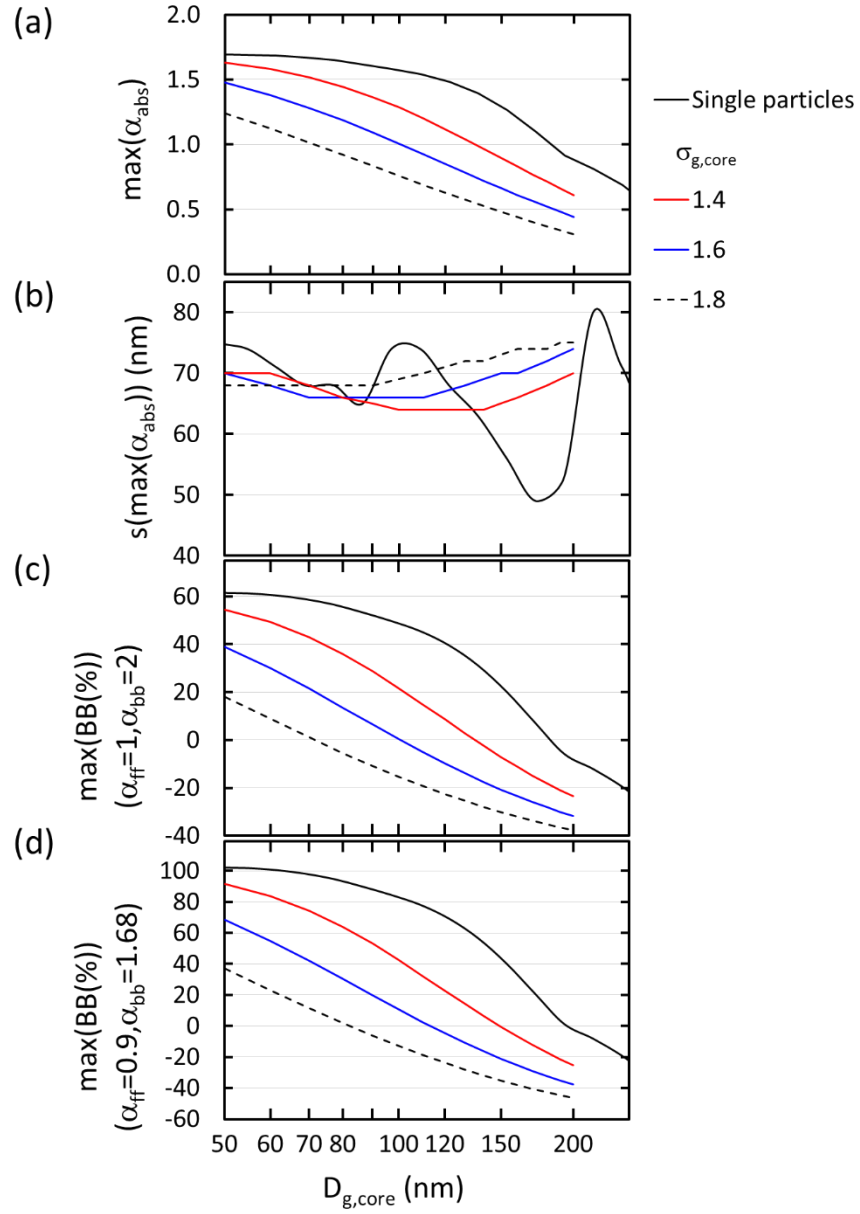


Figure 4. Size distribution dependence of the first maximum of α_{abs} when a size-independent shell grows on a BC core: a) the first maximum value of α_{abs} , b) the shell thickness at the maximum α_{abs} , c) maximum biomass-burning fraction with the Aethalometer model constants $\alpha_{ff} = 1$ and $\alpha_{bb} = 2$, and d) maximum biomass-burning fraction with the Aethalometer model constants $\alpha_{ff} = 0.9$ and $\alpha_{bb} = 1.68$ as a function of the BC core geometric mean diameter ($D_{g,core}$) and geometric standard deviation ($\sigma_{g,core}$).

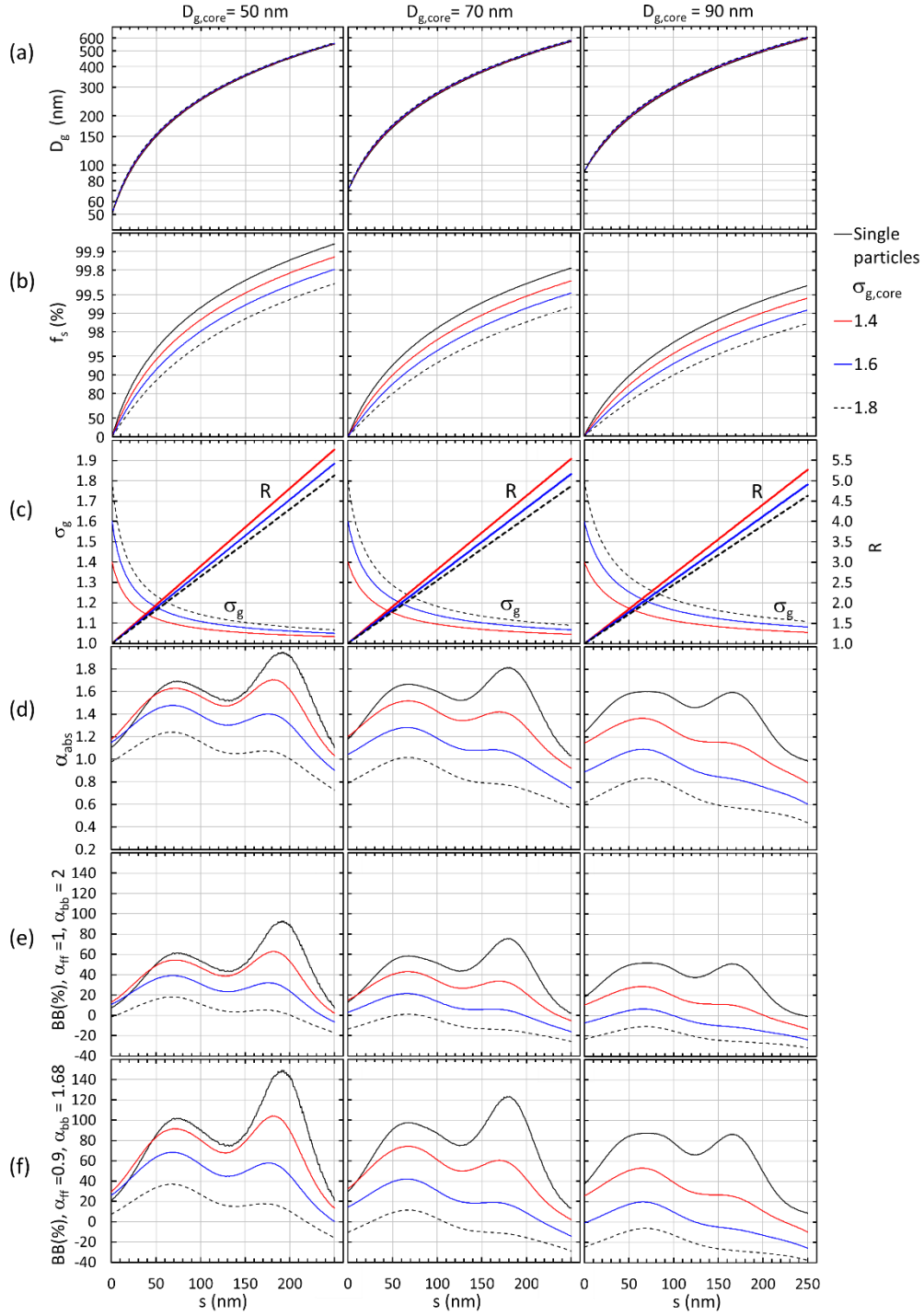
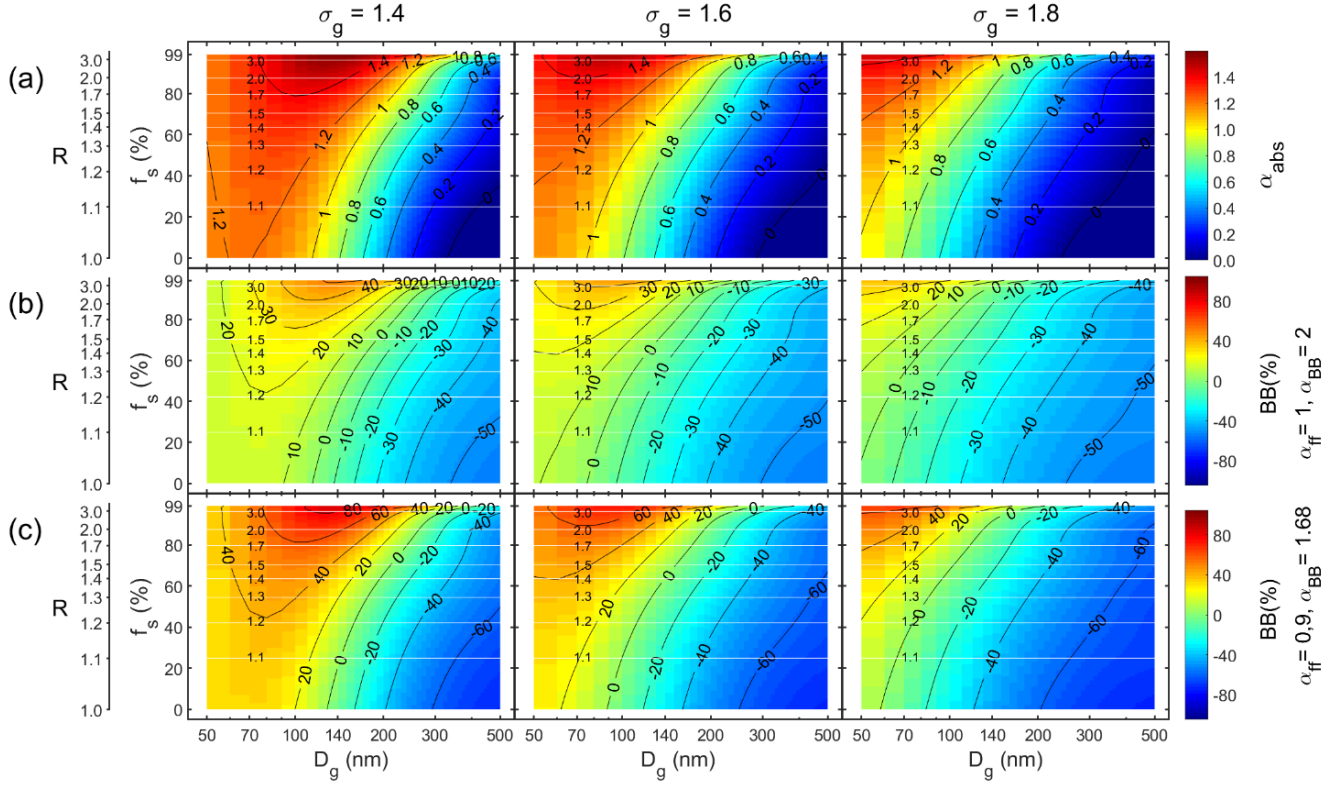
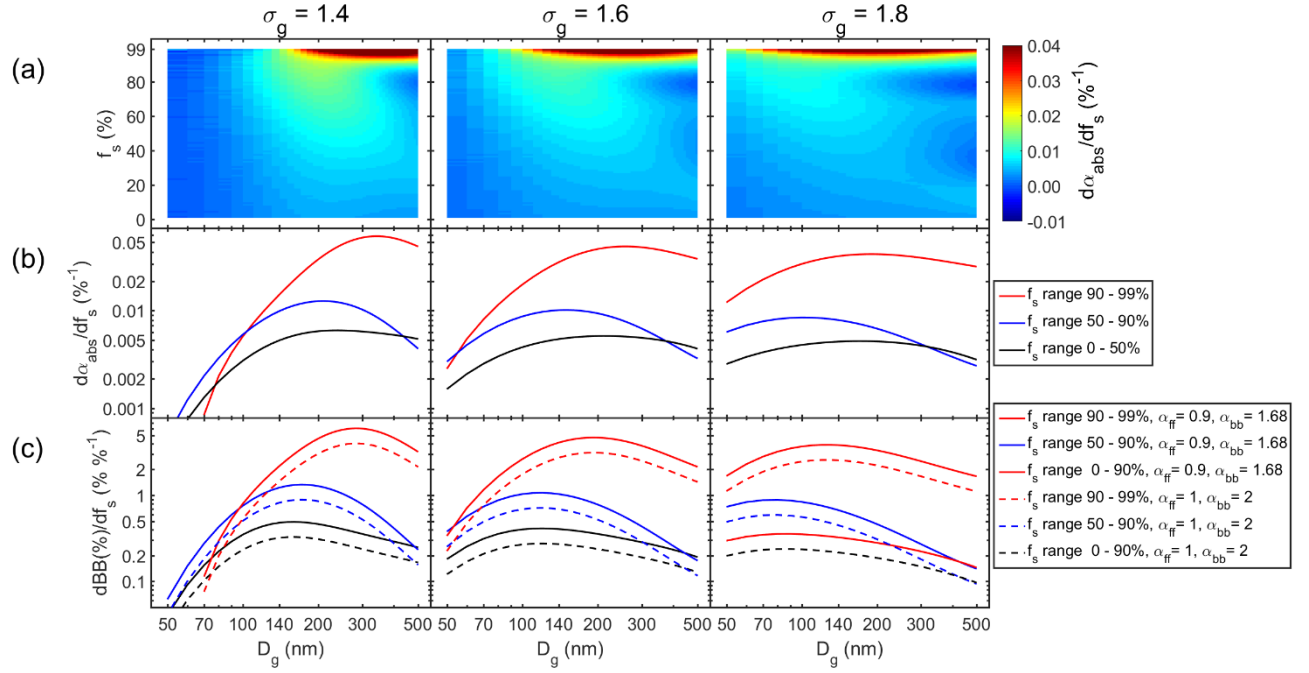


Figure 5. Examples of the growth of a non-size-dependent scattering shell on BC core size distributions with $D_{g,core} = 50$ nm, 70 nm and 90 nm and on single BC particles. a) Geometric mean diameter, b) shell volume fraction, c) geometric standard deviation and D_p -to- D_{core} ratio (R), d) absorption Ångström exponent, e) BB(%) with the Aethalometer model constants $\alpha_{ff} = 1$ and $\alpha_{bb} = 2$, and f) biomass-burning fraction with the Aethalometer model constants $\alpha_{ff} = 0.9$ and $\alpha_{bb} = 1.68$ as a function of shell thickness s .



1

2 Figure 6. Unimodal particle size distributions with size-independent shell volume fractions f_s and three
3 widths of the size distributions: $\sigma_g = 1.4, 1.6$ and 1.8 . a) absorption Ångström exponent (α_{abs}) and the
4 from it calculated fraction of biomass-burning BC ($BB(\%)$) with the Aethalometer model constants of b)
5 $\alpha_{ff} = 1, \alpha_{bb} = 2$ and c) $\alpha_{ff} = 0.9, \alpha_{bb} = 1.68$ vs. the geometric mean diameter of the whole size distribution
6 (D_g). The white horizontal grid lines show constant D_p -to- D_{core} ratios ($= R$).



1

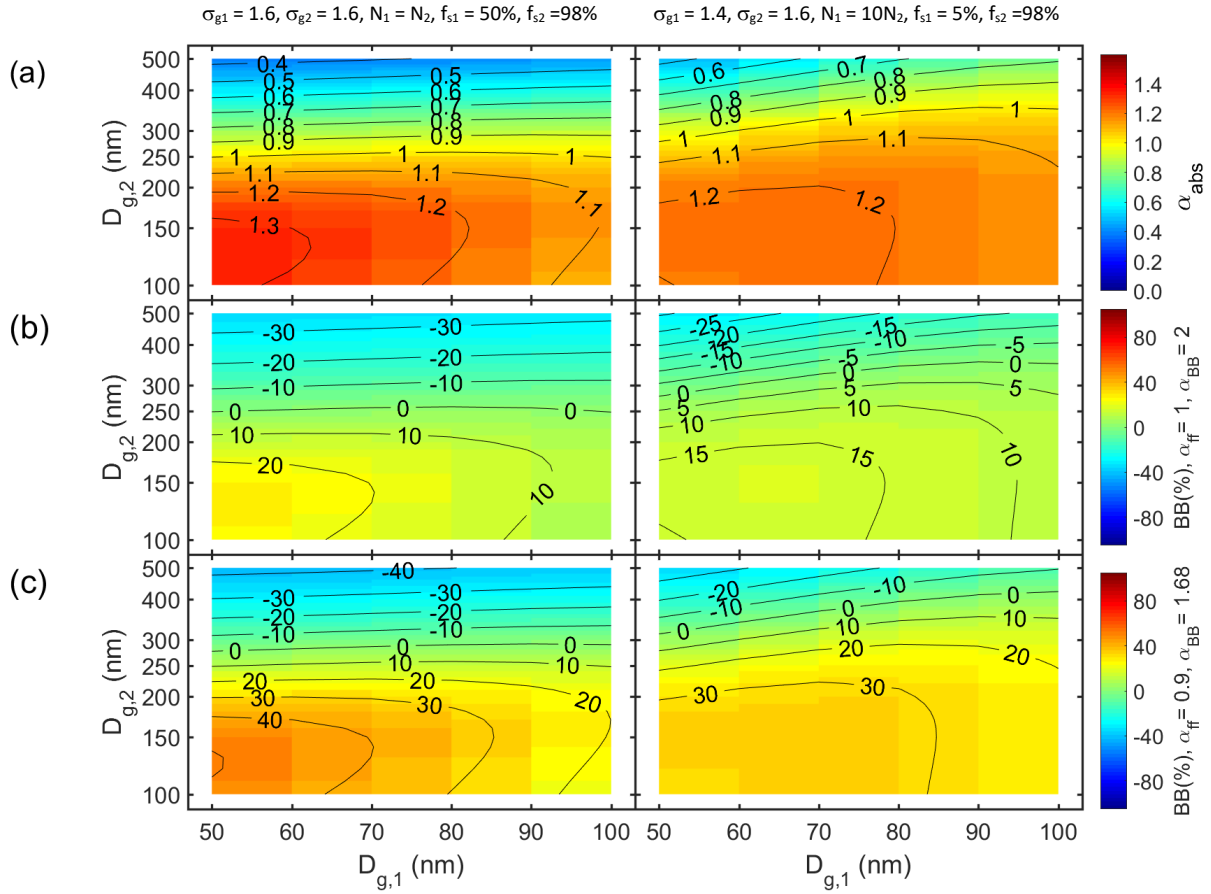
2 Figure 7. Size-dependent sensitivity of α_{abs} and BB(%) to variations of the shell volume fraction f_s . a) α_{abs}

3 sensitivity in the whole f_s range of 1 - 99%, b) average α_{abs} sensitivity in three f_s ranges, and (c) average

4 BB(%) sensitivities in three f_s ranges.

5

1



2

3 Figure 9. Bimodal particle size distributions with size-independent shell volume fractions f_s in two
4 modes as a function of geometric mean diameters of mode 1 (D_{g1}) and mode 2 (D_{g2}). a) absorption
5 Ångström exponent (α_{abs}) and the from it calculated fraction of biomass-burning BC (BB(%)) with the
6 Aethalometer model constants of b) $\alpha_{ff} = 1$, $\alpha_{bb} = 2$ and c) $\alpha_{ff} = 0.9$, $\alpha_{bb} = 1.68$. The widths, the relative
7 number of particles in the two modes and the shell volume fractions of the two modes on the left
8 column: $\sigma_{g1} = 1.6$, $\sigma_{g2} = 1.6$, $N_1 = N_2$, $f_{s1} = 50\%$, $f_{s2} = 98\%$ and on the right column: $\sigma_{g1} = 1.4$, $\sigma_{g2} = 1.6$, N_1
9 $= 10N_2$, $f_{s1} = 5\%$, $f_{s2} = 98\%$.